UAV Flight Height Impacts on Wheat Biomass Estimation via Machine and Deep Learning

Wanxue Zhu ⬤, Ehsan Eyshi Rezaei ⬤, Hamideh Nouri ⬤, Zhigang Sun ⬤, Jing Li, Danyang Yu ⬤, and Stefan Siebert ⬤

Abstract—Optical unmanned aerial vehicle (UAV) remote sensing is widely prevalent to estimate crop aboveground biomass (AGB). Nevertheless, limited knowledge of the UAV flight height (mainly characterized by different image numbers and spatial resolutions) influences the crop AGB estimation accuracy across diverse sensing datasets and machine-/deep-learning models. This article assessed the impacts of flight height and integration of multiscale sensing information on wheat AGB estimation. The multispectral UAV flight missions with 30, 60, 90, and 120 m heights were conducted at the wheat grain filling phase in 2018 and 2019. To estimate AGB, we used the UAV-based crop surface model (CSM), spectral, texture indices, and their combinations along with a deep convolutional neural network (DCNN with AlexNet architecture), random forest, and support vector machine models. Results showed the CSM and textures exhibit sensitivity to flight height, with estimation accuracy declining by 48% and 41%, respectively, as the flight height increased from 30 to 120 m. Spectral indices displayed lesser sensitivity with accuracy decrease of 25%. Integrating data from different heights exhibited better performances in texture and spectral indices while reducing performance when CSM was input. The DCNN performed best particularly at high spatial image scales, whereas more sensitive to flight height, as the AGB estimation accuracy decreased by 30% and 47% from 30 to 120 m for machine learning and DCNN, respectively. Integrating texture and spectral information derived from images with moderate spatial resolutions (4–6 cm), and the integration of multiscale textures, are optimal for grain-filling wheat AGB estimation.

I. INTRODUCTION

IN TEMPERATE zones, wheat (*Triticum aestivum L.*) is the most important staple crop among cereals. Accurately mapping the spatial pattern of wheat aboveground biomass (AGB) is attractive for agronomists who concerns with optimizing crop management for improving grain yield [1]. AGB is defined as the total dry weight of the organic matter aboveground, including leaves, grains, and stems. Destructive sampling is the standard and direct method for AGB measurement. Still, it requires considerable effort and fails to reproduce within-field variability in the biomass caused by soil heterogeneity, topography, and different management or plant diseases [2]. In such a situation, remote sensing, a nondestructive, real-time, and prompt approach, is recognized as a promising alternative for destructive AGB measurement [3], [4]. The classic satellite remote sensing method is mainly devoted to global or regional observations (>1 m resolution), whereas ground-based remote sensing focuses on the individual plant level (<0.01 m resolution) [5], [6]. In terms of precision agriculture, the emergence of unmanned aerial vehicle (UAV) remote sensing provides an opportunity to fill this spatial scale gap, as UAVs can obtain centimeter-level imageries at the field scale via their flexible flight missions [7], [8].

UAV-mounted sensors can capture a wide range of spectral and spatial information about crop canopies [9], [10]. The spectral reflectance of vegetation to specific wavelengths is captured from a broad range of optical cameras. This spectral information which feeds into the machine- and deep-learning algorithms, is the most broadly used data input into the AGB estimation across the environments [11]. However, spectral indices derived from optical images might lose the capability to detect changes in crop growth after canopy closure [3]. Complementary remotely sensed indices have been developed to overcome this challenge and to improve the accuracy of biomass estimations. Optical-based grey level co-occurrence matrix (GLCM) texture is an effective method to characterize the spatial information of canopies, representing the distance and angular spatial relationship over an image subregion of a specific window [12]. The

Wanxue Zhu is with the Institute of Geographic Sciences and Natural Resources Research, Chinese Academy of Sciences, Beijing 100101, China, and also with the Department of Crop Sciences, University of Göttingen, 37075 Göttingen, Germany (e-mail: wanxue.zhu@agr.uni-goettingen.de).

Ehsan Eyshi Rezaei is with the Leibniz Centre for Agricultural Landscape Research, 15374 Müncheberg, Germany (e-mail: ehsaneyshi.rezaei@zalf.de).

Hamideh Nouri is with the Strategy, Science and Corporate Services, Department for Environment and Water, Adelaide, SA 5000, Australia (e-mail: hamideh.nouri@sa.gov.au).

Zhigang Sun is with the Institute of Geographic Sciences and Natural Resources Research, Chinese Academy of Sciences, Beijing 100101, China, also with the College of Resources and Environment, University of Chinese Academy of Sciences, Beijing 100049, China, and also with the Shandong Dongying Institute of Geographic Sciences, Dongying 257000, China (e-mail: sun.zhigang@igsnrr.ac.cn).

Jing Li is with the Institute of Geographic Sciences and Natural Resources Research, Chinese Academy of Sciences, Beijing 100101, China (e-mail: jingli@igsnrr.ac.cn).

Danyang Yu is with the Faculty of Geo-Information Science and Earth Observation, University of Twente, 7500 AE Enschede, The Netherlands (e-mail: d.yu@utwente.nl).

Stefan Siebert is with the Department of Crop Sciences, University of Göttingen, 37075 Göttingen, Germany (e-mail: stefan.siebert@uni-goettingen.de).

Digital Object Identifier 10.1109/JSTARS.2023.3302571

GLCM texture has been widely integrated with spectral information for feature classification [13], estimating crop biomass and yield of rice [14], oilseed rape [4], wheat [3], and maize [15].

Recently, the use of the Structure-from-Motion (SfM) approach via the multiangular imaging of UAV systems has been promoted as another complementary source of information for biomass estimation [16]. The SfM uses highly redundant bundling adjustments based on matching features in multiple overlapping and offsets images solving camera pose and scene geometry [17]. In crop monitoring, SfM develops a crop surface model (CSM)—a raster layer used to extract spatial features of canopy height, which correlates positively with biomass. Several studies have applied CSM and spectral integration data to biomass estimation in maize [2], barley [16], sugarcane [18], and wheat [8]. Precision agriculture experts prefer robust and straightforward approaches for biomass estimation, so it is fundamental to compare the potential of UAV-based CSM and texture datasets in AGB estimation accuracy.

In addition to the fusion of data sources, such as the combination of CSM or textures with spectral data [14], [16], the integration of multiscale data (the "scale" in this article mainly refers to the image spatial resolutions caused by different UAV flight heights) is a potential approach for enhancing the accuracy of crop monitoring, as objects may reflect different features across varying spatial scales [19]. Previous articles have investigated multiscale remote sensing data for wheat monitoring by spatial resampling of images [15]. However, while spatial resampling of images can capture multiscale spectral and texture information, it may not be effective for generating multiscale CSM. This is because CSM is determined not only by spatial resolutions but also by other factors, such as the number of images or image overlap. Spatial resampling cannot add details that were not captured in the original image, which may be critical for accurate biomass estimation. Additionally, due to the spatial heterogeneity of ground features, the scale transformation of remote sensing images might not be appropriate to represent the spatial variability of the field [20]. On the other hand, texture generated by different moving window sizes constitutes another form of multiscale information [3] and has demonstrated its efficacy in enhancing object classification and crop phenotyping accuracy [15], [19].

Despite the extensive use of machine-learning regression for AGB estimation, previous articles have primarily relied on calculating crop canopy features using fixed indices and employed plot average values of each index to represent crop growing conditions [8]. The implementation of a machine-learning model for crop monitoring requires meticulous feature selection that considers specific attributes, such as crop types, growth phases, and ambient conditions. It is imperative to acknowledge that the utilization of feature selection may result in some information loss compared to the raw imagery obtained from UAVs [10], [21]. In comparison, the utilization of deep convolutional neural networks (DCNNs) has demonstrated superior performance in crop phenotyping compared to traditional machine-learning techniques. This is due to the capability of DCNNs to effectively extract abundant features from raw images of crop canopies [7], [22]. However, the impact of image spatial scale on the accuracy of deep learning in AGB estimation is yet to be determined.

On the other side, a low UAV flight height resulted in more imageries and higher ground spatial resolutions, contributing to more feature points and accurately detailed information about observed objects. Therefore, the flight height determines the generation and accuracy of CSM and texture images, thereby affecting the UAV-based remotely sensed canopy features [23]. The high ground spatial resolution of images with dense SfM point clouds leads to higher biomass estimation accuracy [24], [25]. However, a high percentage of across-track overlap and ground spatial resolution of images will increase the flight duration, which has significant implications for data capture and processing costs. Therefore, it is critical to balance the reasonable accuracy of UAV-based monitoring and required costs incorporated with computing/data processing power and time. Liu et al. [23] conducted a series of UAV flight missions with five spatial resolutions (0.4–2.0 cm) to estimate potato biomass. They concluded that the high spatial resolution of images contributed to the better performance of GLCM textures for biomass estimation. It is worth noting that the effects of distinct image resolutions on UAV data performance differed among crops, as crops have different canopy characteristics and cultivation conditions (e.g., ridge and plant density) [26]. Furthermore, most studies combined the remote sensing data to improve machine- and deep-learning models' accuracy in estimating biomass targeting the satellite–UAV combinations [27]. However, whether the integration of multiscale UAV images could improve AGB estimation remains to be elucidated.

This article aims to answer the following research questions: 1) How much does flight height (different ground spatial resolutions of images) affect the wheat AGB estimation accuracy across various UAV datasets (i.e., CSM, texture, spectral, and their combinations)? 2) What is the impact of image spatial scale on the performance of deep learning and machine learning for AGB estimation? 3) Can integration of multiscale UAV data improve the AGB estimation accuracy?

II. MATERIALS AND METHODS

A. Study Area and Experimental Plots

This article was conducted over three experimental sites at the Yucheng Comprehensive Experiment Station of the Chinese Academy of Sciences (36.83° N, 116.57° E), northwestern Shandong Province in the North China Plain (Fig. 1). The Yucheng station is located in a temperate monsoon climate, with average precipitation and air temperature of 582.0 mm and 13.10 °C per year, respectively. The rainy season is between July and September. The cropping pattern is characterized by the double cropping of winter wheat and summer maize. Wheat is sown in early October and harvested in July of the following year.

Three experimental fields were selected for this article. At the nutrient balance experimental site (NBES, Fig. 1), wheat was grown under different nitrogen (N), potash, and phosphate fertilizer supplies and distinct residue management. NBES plots were irrigated at the same level (150–200 mm, adjusted according to the actual rainfall) for each crop season. NBES has 25 plots, each with a size of 5 × 6 m. The experimental site for water–nitrogen–crop relation (WNCR) consists of N-supply and irrigation treatments, including five N levels (N0, N70, N140,
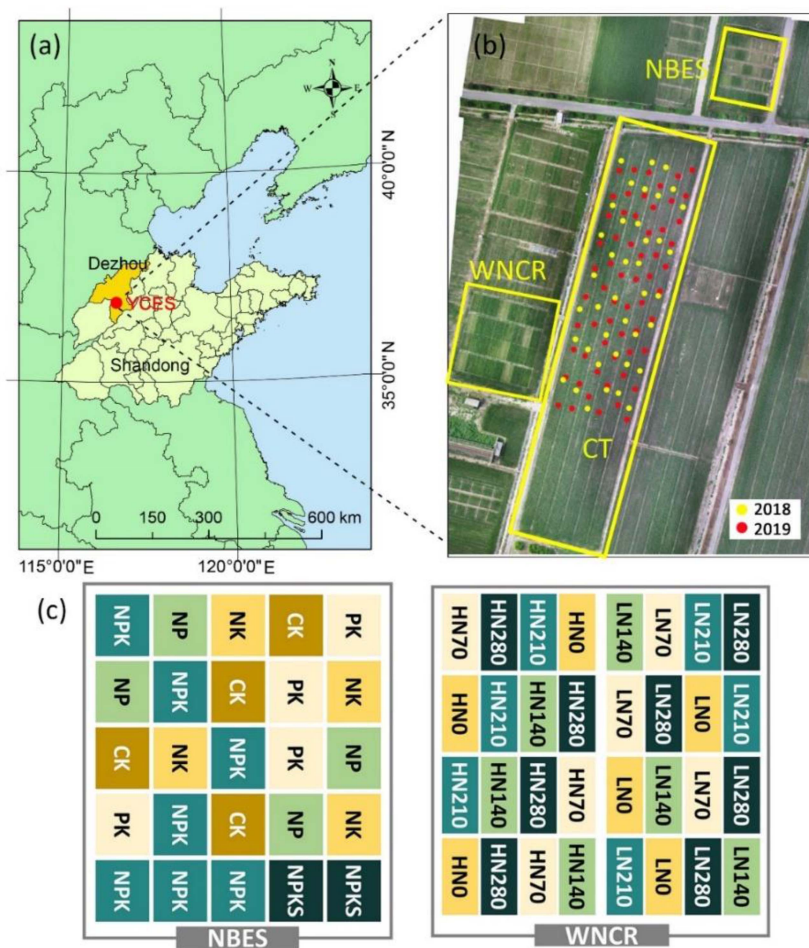
Fig. 1. Location of the Yucheng Comprehensive Experiment Station (YCES) in China (a); overview of the three experimental sites and the sampling points of CT site (b); and specific treatments of experimental sites (c): the nutrient balance experimental site—NBES (CK is no fertilizer; N, P, and K are nitrogen, phosphate, and potash fertilizer supply, respectively; S is returning all residual to the plot) and the water nitrogen crop relation site—WNCR (N0, N70, N140, N210, and N280 are 0, 70, 140, 210, and 280 kg N ha^{-1} for each crop season, respectively; L and H are low—100 mm and high—140 mm irrigation treatments, respectively); the tillage treatment of CT site is the same as that of NBES NPKS plot.

N210, and N280; N70 denotes 70 kg N ha^{-1} for each crop season) and two irrigation levels (140 and 100 mm for high and low irrigation levels, respectively). WNCR has 32 plots, each with a size of 5×10 m. Another experimental site conducted conventional tillage without nutrient or irrigation treatments (denoted as CT site), which is about 60 m $\times$ 200 m; we set the size of CT plots as 10×10 m. The row spacing of wheat planting for all experimental plots was 20 cm.

B. Data Acquisition

The workflow of this article consisted of four major sections (Fig. 2). The data acquisition and preprocessing section include the ground measurement of AGB (Section II-C), acquisition of UAV multispectral images, generation of spectral orthoimages, and digital surface model (DSM) images (Section II-D). Then, generating three UAV datasets, including the spectral, texture, and CSM (derived from DSM) datasets. Extracting spectral, texture, and CSM images of each plot from orthoimages (Section III-A). Next, preparing input data for different algorithms. The clipped images of each plot were used as inputs

of the DCNN model with AlexNet architecture (Section III-B). As for machine learning, the average values of each clipped image were calculated, then the Pearson correlation analysis was conducted to filter highly correlated UAV indicators to avoid multicollinearity (Section II-D). The remaining UAV indicators of each plot were used as inputs of machine-learning models (Section III-B). In this article, random forest (RF) and support vector regression (SVR) were utilized, as these two methods are commonly used and have demonstrated robust performance in previous articles [22], [24]. Running the DCNN, RF, and SVR models to estimate AGB using single-scale (images captured at 30, 60, 90, and 120 m, separately; research question 1) and multiscale (integration of images captured at four heights; research question 3) UAV data, then assessing and analyzing the AGB estimation performance across UAV datasets and models (research question 2, Section III-C).

C. Field Measurements of Wheat

Ground sampling was carried out on the same day after the UAV flight missions. Optimal agronomic management (e.g.,
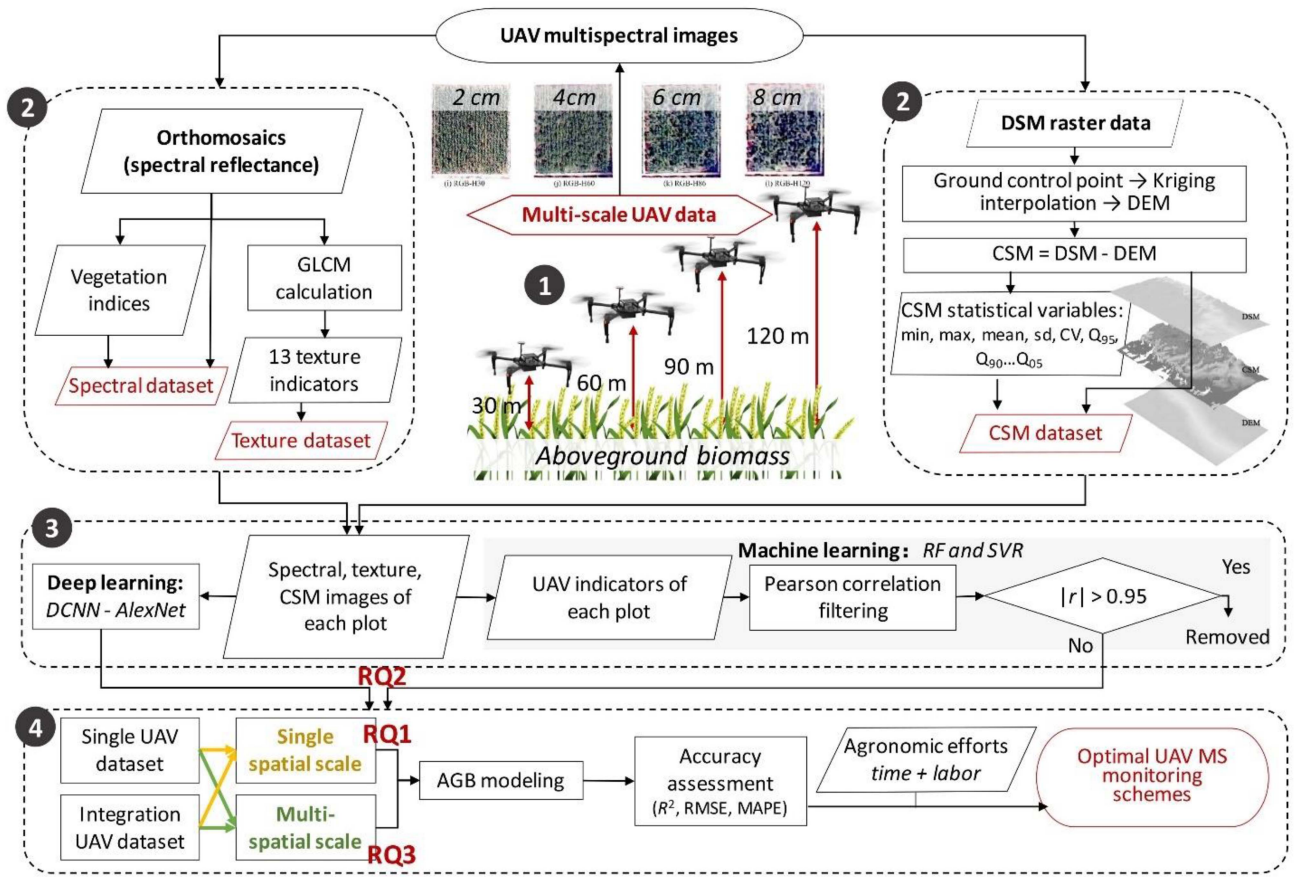
Fig. 2.   Flowchart of this article [UAV = unmanned aerial vehicle; MS = multispectral; AGB = aboveground biomass of wheat; CSM = crop surface model (raster data); DSM = digital surface model (raster data); DEM = digital elevation model (raster data); GLCM = grey level co-occurrence matrix; RF = random forest; SVR = support vector regression; DCNN = deep convolutional neural networks; Q = quantile; and RQ = research question].

weed control) was implemented, focusing on study treatments. Sowing dates for NBES wheat were 15 Oct. 2017 and 7 Oct. 2018, and for WNCR wheat were 9 Oct. 2017 and 12 Oct. 2018. CT wheat sowing was 3 days earlier than NBES. Ground measurements were performed on all WNCR and NBES plots. For CT, 40 and 60 plots were selected for AGB measurement in 2018 and 2019, respectively, with central locations recorded using GPS. Wheat plants in a row of 0.5 m were destructively harvested for lab-based measurement of AGB. These samples were taken at a minimum distance of 50 cm from the plot border to minimize border effects. All the harvested wheat plants were put into envelopes and sent to the laboratory immediately. These samples were dried in an oven at a temperature of 105 °C for 2 h to inactivate enzymes and then at 75 °C to remove the plant moisture until the weight remained constant. For each growing season, 97 and 117 samples of AGB (t·ha^{-1}) were obtained in 2018 and 2019, respectively (Fig. 3).

D. UAV Flight Missions and Data Preprocessing

A MicaSense RedEdge-M multispectral camera (MicaSense, Seattle, WA, USA) onboard a DJI M100 four-rotator UAV (SZ DJI Technology Company, Shenzhen, China) system was used to collect multispectral images. MicaSense has five spectral channels centered at 465–485 nm (blue), 550–570 nm (green), 663–673 nm (red), 712–722 nm (red edge, RE), and 820–860 nm (near-infrared, NIR). The front and side overlaps of the data were 85% and 75%, respectively. Before each flight, the reflectance of spectral panels (with known reflectance) was collected for the subsequent radiation calibration. Two UAV flight missions were executed during the grain filling stage of winter wheat, i.e., 15 May in 2018 and 16 May in 2019. All flight missions were carried out between 11:00 and 13:00 under a clear sky with low wind speed (<5 m·s^{-1}). For each experiment, flight missions with different heights were conducted, including 30, 60, 90, and 120 m, with corresponding spatial resolutions of 2, 4, 6, and 8 cm (1280 × 960 pixels), respectively; hereafter, these datasets were denoted as H30, H60, H90, and H120, respectively.

UAV flight was controlled by the Pix4D Capture (Pix4D, S.A., Lausanne, Switzerland). The preprocessing of MicaSense images was performed using Pix4D Mapper (Pix4D S.A., Lausanne, Switzerland). The initial step involved the evaluation of image quality to ensure adherence to standards. Subsequently, point clouds and mesh were generated to produce three-dimensional SfM point clouds. The final stages included the creation of a DSM in raster format, orthoimages, and spectral indices. A filtering approach was applied to minimize noise and
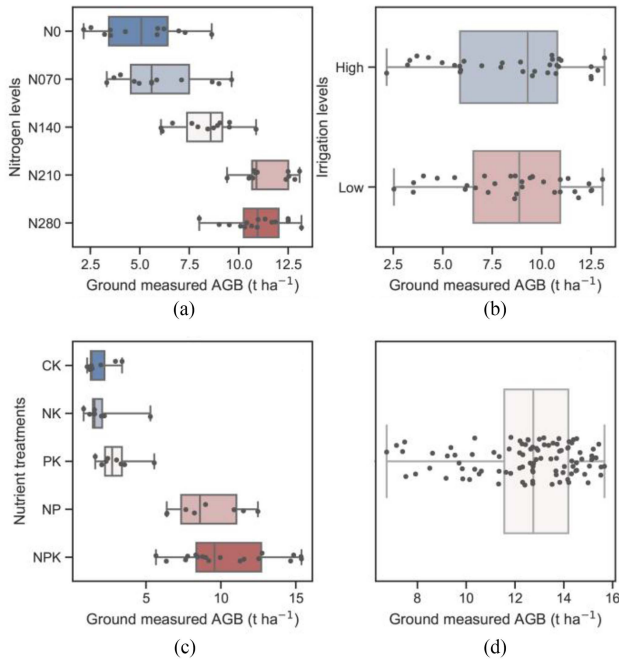
Fig. 3. Box plots of ground measured aboveground biomass (AGB) of wheat in different experimental sites: WNCR with different nitrogen (a) and irrigation (b) levels; NBES (c); CT (d) (the line in each box is the median values of AGB).
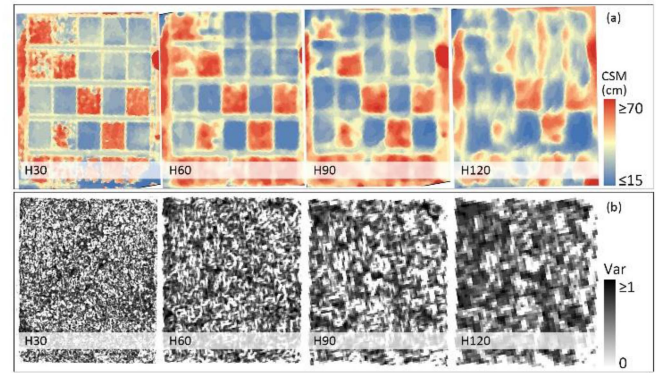

Fig. 4. Examples of the CSM map for the NBES site (a) and the blue band-based variance textures in a fertilized plot of NBES (b) captured at UAV flight heights of 30, 60, 90, and 120 m in the year 2019.

improve the smoothness of the DSM. Spectral panel images were integrated into the initial processing step to calibrate the radiometric values of the generated orthoimages.

III. MODELING FRAMEWORK

A. UAV Dataset Generation and Indicator Screening

Spectral and texture datasets were derived from spectral orthomosaics. The CSM dataset was derived from the DSM images, and calculated as follows:

$$CSM = DSM - DEM \tag{1}$$

where DEM is the digital elevation model (raster), representing the altitude of the soil surface at the experimental site. Based on the supervisory classification, around 100 ground points were selected to extract the values of pixels in the DSM. These selected ground points in DSM were used to generate the DEM using the Kriging interpolation in the QGIS 3.16 (QGIS.org, 2022). Kriging is a regression algorithm for spatial interpolation of stochastic processes based on covariance functions [28]. Then, the CSM [raster, Figs. 2 and 4(a)] could be obtained by subtracting DEM from DSM. The negative values of CSM pixels were set to Null to remove the impact of errors. The use of a consistent UAV image processing chain in this article ensured that the spatial resolution of the CSM remained constant at 20 cm for all four UAV flight heights.

Texture variables [Figs. 2 and 4(b)] were calculated using the GLCM [29] via the *r.texture* tool in the QGIS. Thirteen texture variables were calculated for each band: the first-order statistics in the spatial domain calculated seven texture variables, including the sum average, entropy, difference entropy, sum entropy,

variance, difference variance, and sum variance; the second-order statistics calculated six texture variables, including the angular second moment, inverse difference moment, contrast, correlation, information measures of correlation, and maximal correlation coefficient. The moving window for texture calculation was set to 3×3 (default). The spectral dataset includes the reflectance values of the five bands and their vegetation indices calculated from the reflectance (Table I). Considering the spectral channels of the MicaSense camera, 12 commonly used vegetation indices of each pixel were calculated using Python 3.9.

Since UAV flights at four heights were conducted, each dataset has four subdatasets generated from images captured at each height. Considering plot sizes and border areas, squares of 4.48 m $\times$ 4.48 m were selected for the extraction of UAV indicators (e.g., 224×224 pixels for UAV data with 2 cm as spatial resolution) using the ROI tool of ENVI 5.5 (Exelis Visual Information Solutions, Boulder, CO, USA).

In total, 1, 65, and 17 types of CSM, texture, and spectral images were generated in this article for deep-learning inputs, respectively. As for the machine-learning approach, the mean values of each selected region were calculated to represent the plot-level indicators. The statistical variables of CSM pixels within a plot were calculated using Python 3.9, including the minimum, mean, maximum, standard deviation, coefficient of variation, and quantile values (mean values of the top 95%, 90%, …, 5%, denoted as Q_{95}, Q_{90}, … Q_5). Then, the Pearson correlation analysis was carried out to filter highly correlated UAV variables ($|r| > 0.95$, $p < 0.01$) of each dataset using the *findCorrelation* functions of the R language [11]. The number of variables retained from the UAV dataset after filtering at various flight heights was 10, 31, and 8 for spectral, texture, and CSM datasets, respectively. The machine-learning approach utilized these retained variables as inputs to ensure consistency in estimation across various flight heights.

B. Models for Aboveground Biomass Estimation

Deep learning: A DCNN using AlexNet architecture was employed in this article [32], and DCNN has been proven effective in estimating crop AGB in our previous articles [22].

TABLE I
VEGETATION INDICES USED IN THIS ARTICLE

Vegetation indices	Formulas [1]	References
Normalized difference vegetation index (*NDVI*)	*(NIR − R)/(NIR + R)*	[10]
Red edge NDVI (*NDRE*)	*(NIR −RE)/(NIR + RE)*	
Green NDVI (*GNDVI*)	*(NIR − G)/(NIR + G)*	[30]
Simple Ratio (*SR*)	*NIR/R*	[31]
Red edge reflectance ratio (*SRRE*)	*NIR/RE*	
Ratio vegetation index (*RVI*)	*NIR/G*	[4]
Soil adjusted vegetation index (*SAVI*)	*1.5[(NIR−R)/(NIR+R+0.5)]*	[30]
Modified SAVI (*MSAVI*)	$0.5(2NIR$ $-\sqrt{(2NIR+1)^2 - 8(NIR-R)})$	[10]
Optimized soil adjusted vegetation index (*OSAVI*)	*1.16(NIR-R)/ (NIR+R+0.16)*	
Enhanced vegetation index (*EVI*)	*2.5[(NIR−R)/(NIR+6R−7.5B + 1)]*	
Chlorophyll index green (*CIG*)		
Improved chlorophyll absorption ratio index (*MCARI*)	*(RE–R)–0.2(RE–G)(RE/R)*	[30]

[1] The *B, G, R, RE*, and *NIR* represent the spectral reflectance of the blue, green, red, red edge, and near-infrared bands, respectively.
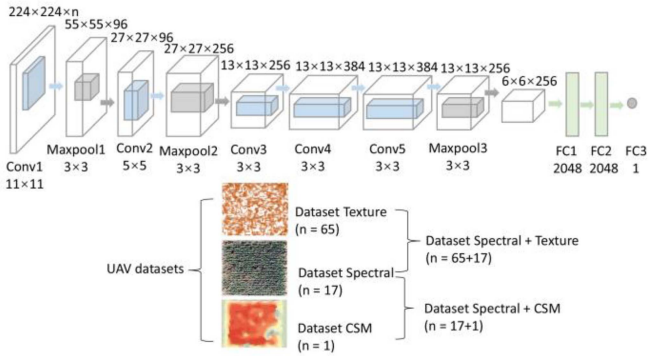

Fig. 5. Architecture of the AlexNet DCNN (FC is the fully connected layer; Conv is the convolutional layer; taking the input size of 224×224 pixels as an example).

The AlexNet has five convolutional, three maxpool, and three fully connected layers (Fig. 5). AlexNet uses the nonsaturating ReLU activation function, overperforming the Tanh and Sigmoid approaches regarding model training. The dimension of input images is affected by spatial resolution and dataset channels. As deep learning needs no feature filtering, the channels equal 1, 17, and 65 for CSM, spectral, and texture datasets, respectively. Here, although more CSM variables were calculated in Section III-A, these CSM variables are not raster images but the average values of each plot, which cannot be the DCNN inputs. Therefore, the channel of the CSM dataset was set to one. As for the spectral + CSM dataset, the channel should be the sum of 17 and 1, and other integration datasets follow this rule (Fig. 5). The DCNN was implemented using the PyTorch deep-learning framework.

Machine learning: Before modeling, all UAV indicators were normalized to mean and standard deviation values of 0 and 1, respectively, using the *scale* function in R. The RF is a classifier consisting of a collection of tree-structured classifiers where the values of a random vector are sampled independently, and all the trees have the same distribution. The tree predictor takes on numerical values to achieve the regression, and the correct type of randomness injection makes RF an accurate regressor [33].

This article carried out the RF model using the *randomForest* R package, including two critical parameters, i.e., *mtry* and *ntree*. The *mtry* is the number of variables randomly sampled as candidates at each split, set to 3 (default). The *ntree* is the number of trees to grow, and the minimum error determines its optimal values [34].

Support vector machine solves binary classification problems by formulating them as convex optimization problems, which entails finding the maximum margin separating the hyperplane (support vectors) while correctly classifying as many training points as possible. The generation of support vector machine to SVR is accomplished by introducing an ε-tube which is an intensive region around the function. SVR is characterized by kernels, sparse solution, and Vapnik–Chervonenkis control of the margin and the number of support vectors [35]. This article carried out the SVR modeling via the *e1071* R package.

C. Modeling and Accuracy Assessment

The AGB estimation of this article includes three sections using: 1) spectral, texture, and CSM datasets captured at different heights; 2) the data integrated datasets: spectral + CSM and spectral + texture captured at different flight heights; and 3) the scale-integrated datasets, i.e., the integration of H30, H60, H90, and H120 datasets. To investigate the transferability of models across years for better serving generalization of results across various environments, as well as considering sampling size, the data from 2019 and 2018 were utilized for model training and validation, respectively. The validation was quantified by three statistical indicators, including the coefficient of determination (R^2), root mean square error (*RMSE*, t·ha^{-1}), and mean absolute percentage error (*MAPE*, %) using the following equations:

$$R^2 = \left\{ \left[\sum_{i=1}^{n} \left(Y_i - \bar{Y}\right)\left(E_i - \bar{E}\right) \right] \middle/ \left[\sqrt{\sum_{i=1}^{n} \left(Y_i - \bar{Y}\right)^2} \sqrt{\sum_{i=1}^{n} \left(E_i - \bar{E}\right)^2} \right] \right\}^2 \tag{2}$$

TABLE II
ACCURACY ASSESSMENT OF WHEAT AGB ESTIMATION (VALIDATION, $N = 97$) USING UAV SENSING SPECTRAL, TEXTURE, AND CSM DATASETS CAPTURED AT FOUR FLIGHT HEIGHTS

Dataset	Model[1]	R^2			$RMSE$ (t·ha^{-1})			$MAPE$ (%)		
		Spec	Text	CSM	Spec	Text	CSM	Spec	Text	CSM
H30	RF	0.71	0.72	0.72	2.15	2.08	2.13	25.3	24.7	22.8
	SVR	0.72	0.69	0.73	2.16	2.18	2.15	23.5	24.2	22.9
	DCNN	0.78	0.74	0.75	1.85	2.0	2.00	21.7	22.7	20.3
H60	RF	0.70	0.64	0.59	2.27	2.46	2.49	25.0	23.4	34.2
	SVR	0.71	0.61	0.59	2.25	2.58	2.54	24.9	23.5	34.4
	DCNN	0.73	0.72	0.65	2.12	2.12	2.33	24.6	21.0	32.3
H90	RF	0.65	0.54	0.49	2.43	2.83	2.87	29.1	26.8	40.0
	SVR	0.62	0.52	0.43	2.55	2.85	3.11	30.5	27.0	44.4
	DCNN	0.66	0.55	0.55	2.49	2.78	2.73	25.4	28.9	40.5
H120	RF	0.63	0.55	0.34	2.48	2.77	3.17	30.0	26.8	55.7
	SVR	0.63	0.49	0.38	2.49	2.98	3.08	29.6	29.0	58.2
	DCNN	0.61	0.48	0.39	2.66	3.04	3.01	28.3	33.1	58.0

[1]RF is random forest; SVR is support vector regression; and DCNN is the deep convolutional neural network using the AlexNet architecture.

$$RMSE = \sqrt{\sum_{i=1}^{n} (Y_i - E_i)^2 / n} \qquad (3)$$

$$MAPE = 100\% \times \left(\sum_{i=1}^{n} |Y_i - E_i| / Y_i \right) / n \qquad (4)$$

where i is the sequence number of the array, Y_i is the AGB value (t·ha^{-1}) of the measured AGB array, E_i is the AGB value of the estimated AGB array, $\bar{Y}$ represents the average value of the measured AGB array, and $\bar{E}$ is the average value of the estimated AGB array.

The changes in AGB estimation accuracy comparison are calculated as follows:

$$CEA = 100\% \times (X / X_0 - 1) \qquad (5)$$

where CEA is the changes in AGB estimation accuracy (%); X and X_0 are the target and reference AGB estimation accuracy indicators, respectively, i.e., R^2, RMSE, and MAPE. To assess the impact of image spatial scale on AGB estimation, X and X_0 were used as accuracy indicators for the H120 and H30 datasets, respectively. The integration of texture or CSM with spectral datasets was analyzed by comparing the efficiency indicators X and X_0 for spectral + texture (or + CSM) and spectral datasets, respectively. The contribution of image spatial scale integration on AGB estimation was evaluated by comparing the accuracy indicators X and X_0 for the scale-integrated and H30 datasets, respectively.

IV. RESULTS

A. Aboveground Biomass Estimation Using UAV Single Datasets at Different Scales

The accuracy of AGB estimation across different UAV datasets showed that R^2 were 0.61–0.78, 0.48–0.74, and 0.34–0.75; RMSE were 1.85–2.66, 2.0–3.04, and 2.0–3.17 t·ha^{-1}; and MAPE were 22%–31%, 21%–33%, and 20%–58% for spectral, texture, and CSM datasets, respectively (Table II). As exemplified by the results from the DCNN, AGB was overestimated

in low values and underestimated in high values using CSM datasets at H90 and H120, whereas the spectral and texture data did not exhibit such tendencies (Fig. 6). From H30 to H120 datasets, the average R^2 values of spectral, texture, and CSM-based estimation decreased by 15%, 30%, and 50%; RMSE increased by 25%, 41%, and 48%; and MAPE increased by 25%, 25%, and 162%, respectively (Table III). These findings demonstrate that the performance of the spectral dataset was less impacted by variations in image spatial scale, while the performance of the CSM dataset was the most sensitive to changes in image scale.

Comparing models, the RMSE values of RF, SVM, and DCNN-based estimation were 2.08–3.17, 2.15–3.11, and 1.85–3.04 t·ha^{-1}, respectively, with corresponding R^2 values of 0.34–0.72, 0.38–0.73, and 0.39–0.78, respectively (Table II). The results showed that the H30 scale was the most accurate when comparing machine-learning and DCNN methods, and the out-performance of DCNN over machine learning was obvious at the H30 scale. However, the three models showed similar performance at H120. The superiority of DCNN at high image spatial resolution could not overcome the limitations of coarse spatial resolution images, and DCNN was more sensitive to image scales than RF and SVM methods. The RMSE changes between H30 and H120 were 49%, 32%, and 33% for DCNN, SVM, and RF methods, respectively (Table III).

B. Aboveground Biomass Estimation Using UAV Combined Datasets at Different Scales

As shown in Table IV and Fig. 7, the integration of spectral data with textures was superior to that with CSM. The integration of spectral data with textures showed a decrease of 16.6% in R^2, an increase of 24.1% in RMSE, and an increase of 29.1% in MAPE from H30 to H120 datasets (Table V). Conversely, the integration of spectral data with CSM showed a decrease of 36.6% in R^2, an increase of 48.1% in RMSE, and an increase of 78.0% in MAPE from H30 to H120 datasets (Table V). These results demonstrated that the high spatial resolution of UAV images contributed to AGB estimation, and the image scales
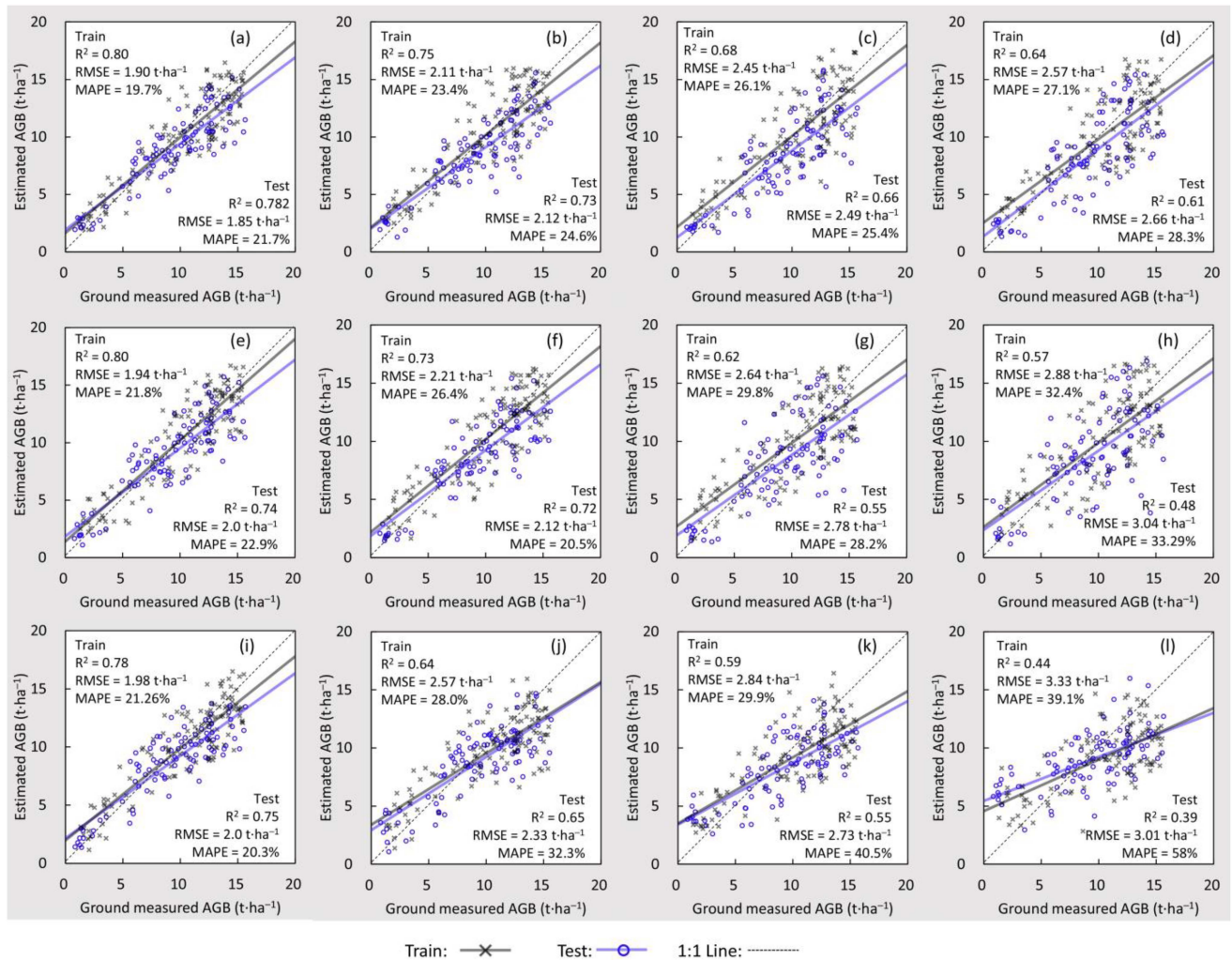
Fig. 6. Ground measured versus estimated wheat AGB (t·ha^{-1}) using UAV spectral datasets at H30 (a), H60 (b), H90 (c), and H120 (d); using texture datasets at H30 (e), H60 (f), H90 (g), and H120 (h); and using CSM datasets at H30 (i), H60 (j), H90 (k), and H120 (l) [train and test are the accuracy assessment of training (data in 2019) and testing (data in 2018) models, respectively].

TABLE III
CHANGES OF AGB ESTIMATION ACCURACY USING UAV SENSING SPECTRAL, TEXTURE, AND CSM DATA FROM H30 TO H120[1]

Model	R^2 changes (%)				RMSE changes (%)				MAPE changes (%)			
	Mean[1]	Spec	Text	CSM	Mean	Spec	Text	CSM	Mean	Spec	Text	CSM
RF	−29.7	−11.9	−23.8	−53.5	32.7	15.6	33.3	49.1	57.1	18.5	8.1	145
SVR	−29.6	−11.7	−29.0	−48.0	31.9	15.6	36.8	43.2	66.8	26.3	19.7	154
DCNN	−35.0	−22.2	−35.3	−47.6	48.9	43.9	52.2	50.6	87.4	30.3	45.6	186
Mean		−15.3	−29.4	−49.7		25.0	40.8	47.6		25.0	24.5	162

[1] The mean is calculated by the results of different datasets or models. For example, the mean R^2 change of the RF model is −29.7%, calculated by the average of −11.9% (spectral), −23.8% (texture), and −53.5% (CSM).

had more influence on the performance of spectral + CSM than spectral + texture datasets in AGB estimation, which can also be observed from Fig. 7.

Comparing dataset integration performance, the RMSE of spectral + texture-based estimation decreased by 3.13%–15.4%, and MAPE decreased by 0.31%–27.2%, suggesting the integration of texture into spectral datasets could improve AGB estimation accuracy at four flight heights (Table VI). As for

the integration of CSM and spectral, the AGB estimation accuracy increased at H30 with higher R^2, lower RMSE and MAPE values; while in H60, H90, and H120 datasets, the R^2 decreased by 3.12%–26.0% and MAPE increased by 1.6%–47.3% (except for DCNN at H60, Table VI). These results indicated that integrating CSM derived from images with high (2 cm in this article) resolution into spectral could improve AGB estimation accuracy, while integrating CSM from medium
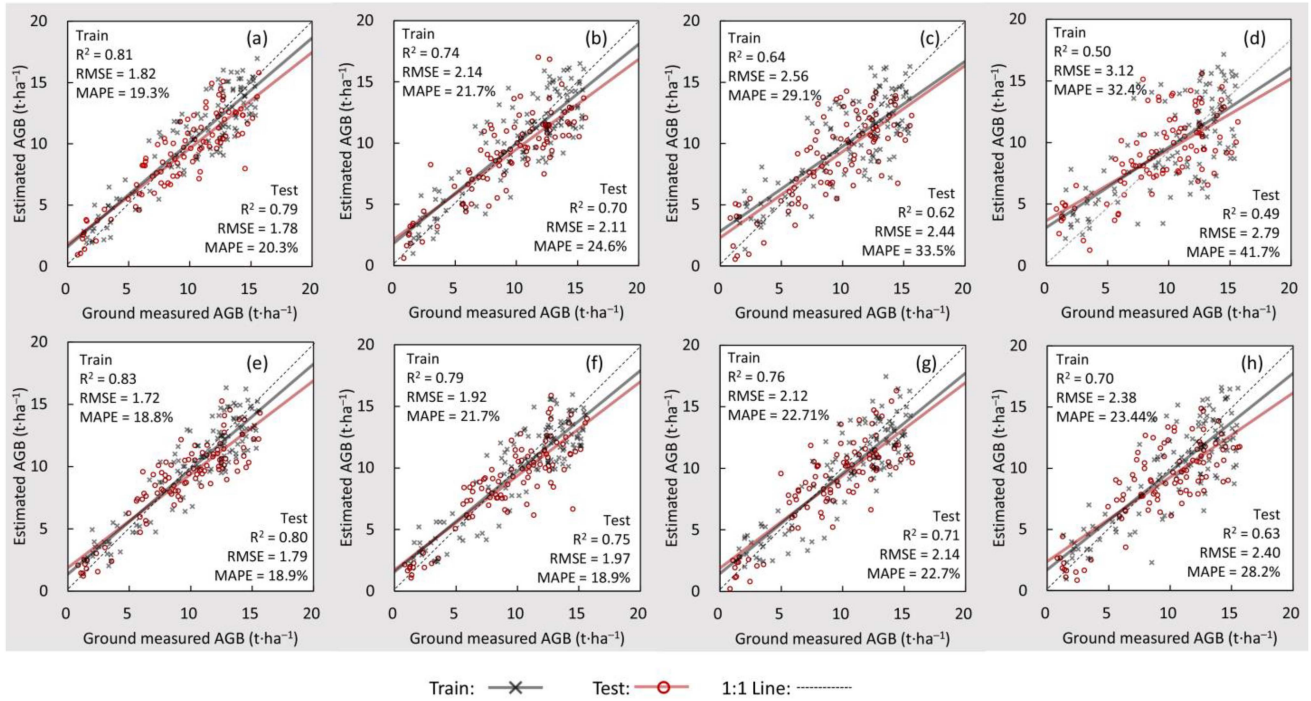
Fig. 7. Ground measured versus estimated wheat AGB (t·ha^{-1}) using UAV spectral + CSM datasets at H30 (a), H60 (b), H90 (c), and H120 (d); using spectral + texture datasets at H30 (e), H60 (f), H90 (g), and H120 (h).

TABLE IV
ACCURACY ASSESSMENT OF WHEAT AGB ESTIMATION (VALIDATION, $N = 97$) USING UAV SENSING SPECTRAL + TEXTURE DATASET CAPTURED AT FOUR FLIGHT HEIGHTS

Dataset	Model	R^2		RMSE		MAPE	
		+Text[1]	+CSM	+Text	+CSM	+Text	+CSM
H30	RF	0.76	0.75	2.02	1.96	23.7	24.5
	SVR	0.74	0.73	2.0	2.05	22.5	23.6
	DCNN	0.80	0.79	1.79	1.78	18.9	20.3
H60	RF	0.73	0.65	2.12	2.29	24.0	29.2
	SVR	0.70	0.66	2.14	2.27	22.6	28.1
	DCNN	0.75	0.70	1.97	2.11	18.9	24.6
H90	RF	0.69	0.63	2.25	2.38	23.7	29.6
	SVR	0.71	0.59	2.16	2.59	22.2	31.5
	DCNN	0.71	0.62	2.14	2.44	22.7	33.5
H120	RF	0.64	0.48	2.44	2.82	28.1	36.9
	SVR	0.65	0.47	2.34	2.95	26.9	42.0
	DCNN	0.63	0.49	2.40	2.79	28.2	41.7

[1] The +Text and +CSM datasets are spectral + texture and spectral + CSM datasets, respectively.

TABLE V
CHANGES OF AGB ESTIMATION ACCURACY USING UAV SENSING SPECTRAL + TEXTURE AND SPECTRAL + CSM DATASETS FROM 30 TO 120 M

	Model	RF	SVR	DCNN	Mean
R^2 change (%)	Mean	−26.3	−24.1	−29.3	
	+Text	−16.6	−12.0	−21.1	−16.6
	+CSM	−36.0	−36.2	−37.5	−36.6
RMSE change (%)	Mean	32.4	30.5	45.3	
	+Text	20.5	17.2	34.5	24.1
	+CSM	44.4	43.8	56.1	48.1
MAPE change (%)	Mean	34.5	48.8	77.4	
	+Text	18.4	19.8	49.2	29.1
	+CSM	50.6	77.8	105.6	78.0

the performance of the three models was comparable. The results suggest that DCNN is more sensitive to image spatial scales than RF and SVM, and algorithm superiority cannot compensate for shortcomings in image spatial scales.

C. Aboveground Biomass Estimation Using Scale-Integrated UAV Datasets

The results of the scale-integrated spectral, texture, and spectral + texture datasets showed a high level of accuracy in estimating AGB, as evidenced by the R^2 values ranging from 76% to 80%, 71% to 80%, and 77% to 84%, respectively (Table VII). On the other hand, the performance of the scale-integrated CSM and spectral + CSM datasets was moderate, with R^2 values ranging around 0.60. Among all the datasets, the spectral + texture

to coarse images (4–8 cm in this article) would decrease model accuracy.

The R^2 values were 0.48–0.76, 0.47–0.74, and 0.49–0.80 and corresponding RMSE were 1.96–2.82, 2.0–2.95, and 1.78–2.79 t·ha^{-1} for RF, SVR, and DCNN, respectively (Table IV). DCNN was superior to machine-learning methods at high spatial resolution (H30), with R^2, RMSE, and MAPE of 0.80, 1.79 t·ha^{-1}, and 19% compared to 0.75, 2.0 t·ha^{-1}, and 23% for machine-learning methods. However, at H90 and H120 scales,

TABLE VI
CHANGES OF AVERAGE AGB ESTIMATION ACCURACY AFTER INTEGRATING
CSM OR TEXTURE INTO THE SPECTRAL DATASET

Dataset	Model	R^2 change (%)		RMSE change		MAPE change	
		+Text	+CSM	+Text	+CSM	+Text	+CSM
H30	RF	7.30	5.69	−5.70	−8.88	−6.46	−3.34
	SVR	3.10	2.34	−7.28	−4.76	−4.08	0.74
	DCNN	2.21	0.64	−3.13	−3.31	−13.0	−6.69
H60	RF	3.44	−7.98	−6.30	0.95	−4.19	16.8
	SVR	−2.62	−8.09	−4.87	0.80	−9.39	12.7
	DCNN	3.41	−3.12	−7.17	−0.42	−23.4	−0.31
H90	RF	6.60	−3.54	−7.26	−2.04	−18.5	1.60
	SVR	14.96	−5.62	−15.4	1.57	−27.2	3.14
	DCNN	6.37	−6.23	−14.2	−2.07	−10.4	32.2
H120	RF	1.54	−23.3	−1.71	13.8	−6.56	22.9
	SVR	2.79	−26.0	−6.02	18.5	−9.02	41.9
	DCNN	3.64	−19.1	−9.48	4.88	−0.31	47.3

TABLE VII
ACCURACY ASSESSMENT OF WHEAT AGB ESTIMATION (VALIDATION, $N = 97$)
USING SCALE-INTEGRATED UAV SENSING DATASETS

	Model	Spectral	Text	CSM	+Text	+CSM
R^2	RF	0.77	0.76	0.57	0.82	0.64
	SVR	0.76	0.71	0.52	0.77	0.61
	DCNN	0.80	0.80	0.58	0.84	0.65
RMSE	RF	2.07	2.16	2.68	1.96	2.49
(t·ha⁻¹)	SVR	1.95	2.14	2.74	1.99	2.51
	DCNN	1.75	1.83	2.71	1.68	2.33
MAPE	RF	24.16	20.13	30.81	20.24	27.52
(%)	SVR	20.58	20.31	30.54	18.86	27.04
	DCNN	20.59	16.98	28.84	16.59	26.86

TABLE VIII
CHANGES OF AGB ESTIMATION ACCURACY (%) AFTER INTEGRATING
MULTISCALE UAV DATA

	Model	Spectral	Text	CSM	+Text	+CSM
R^2	RF	7.92	4.92	−21.8	8.02	−14.6
change	SVR	6.31	3.24	−28.3	4.63	−17.1
	DCNN	2.47	8.32	−23.2	5.33	−17.9
RMSE	RF	−3.68	3.67	26.0	−3.02	27.2
change	SVR	−9.31	−1.79	27.5	−0.44	22.3
	DCNN	−5.07	−8.36	35.7	−5.75	30.43
MAPE	RF	−4.62	−18.6	35.4	−14.6	12.4
change	SVR	−12.2	−16.2	33.5	−16.2	14.5
	DCNN	−5.17	−25.3	42.4	−12.2	32.6

datasets showed the best performance in AGB estimation, with a DCNN-based R^2 value of 0.84, RMSE of 1.68 t·ha⁻¹, and MAPE of 16.6% (Table VII).

Comparing the scale-integrated and H30 datasets, the integration of multiscale images improved the estimation accuracy of the spectral, texture, and spectral + texture datasets, as their R^2 increased by 2.5%–7.9%, 3.2%–8.3%, and 4.6%–8.0%, respectively, and MAPE decreased by around 7%, 20%, and

15%, respectively (Table VIII). However, scale integration decreased the estimation accuracy of CSM and spectral + CSM datasets, as their RMSE values increased by around 30% and 25%, respectively. Additionally, the DCNN model showed a slightly improved performance in comparison to the RF and SVR algorithms when utilizing the scale-integrated UAV datasets. However, there were no substantial variations observed in the accuracy of AGB estimation among the models.

V. DISCUSSION

A. Factors Affecting the Performance of UAV Datasets

CSM performance—The accuracy of SfM point clouds determines the performance of CSM in AGB estimation. The SfM is mainly affected by UAV flight design (e.g., image overlap, flight height, and route), sensor quality and calibration, algorithms of SfM generation, georeferencing strategy, and illumination changes [36], [37]. In flight design, the front/forward overlap of images plays a vital role in SfM point cloud penetration and accuracy. The 90% stereo overlaps could detect forest ground in the canopy gaps, while the 60% overlap could roughly detect half the depth into canopy gaps [17], [38]. Although high image overlap ensures a stable image connection for the subsequent aerial triangulation, which contributes to accurate vegetation height and biomass detection [17], [25], the excessive overlap of images decreases the monitoring coverage and increases the computation burden. This tradeoff should be carefully evaluated to fit the purpose of agroapplications.

This article focused more on the flight height that the users usually set according to specific purposes. As elevated objects observed under distinct view angles have different radiometric features [36], low flight height captures more images with varying view angles within the region of interest, providing accurate information in feature matching. On the other hand, high spatial resolution with low flight height provides pure pixels vital for detecting objects' features, which is also recognized in previous articles [39], [40]. Therefore, the number of involved images captured from different angles and their spatial resolutions play vital roles in SfM quality, leading to the high sensitivity of CSM performance to UAV flight height in AGB estimation.

The performance of CSM is influenced by several factors, including the relationship between AGB and the information derived from CSM. CSM can capture the vertical structure of the canopy, making it widely used for estimating vegetation height and crown diameter. Crop height has been found to have a strong correlation with AGB, which allows for accurate estimation using SfM point clouds-generated CSM [24]. Although the biomass of wheat plants is proportional to the intercepted photosynthetically active radiation, which is influenced by multiple factors, primarily canopy architecture, and vegetation greenness [41], [42], [43]. Consequently, it is challenging to estimate crop biomass using the single aspect of crop height conveyed in CSM, especially under environmental stress conditions. As demonstrated in Table IX, the correlations (|r| values) between CSM variables and AGB declined by approximately 50% when comparing the distances of 30 and 120 m. This observation helps to explain the aforementioned issue.

TABLE IX
RELATIONSHIPS ($|r|$ VALUES, $N = 214$) BETWEEN AGB AND UAV VARIABLES[1] ACROSS SPATIAL SCALES

Variables[2]	H30	H60	H90	H120
CSM-mean	0.73	0.63	0.49	0.41
CSM-Q_{80}	0.72	0.62	0.53	0.35
CSM-Q_{90}	0.70	0.55	0.45	0.30
Text-COR	0.74	0.62	0.54	0.51
Text-MEAN	0.69	0.70	0.64	0.54
Text-ENT	0.71	0.63	0.64	0.61
Spec-MCARI	0.75	0.74	0.61	0.64
Spec-NDRE	0.75	0.66	0.72	0.54
Spec-SRRE	0.68	0.72	0.61	0.56

[1] Three UAV variables of each dataset were shown, considering the corresponding Pearson correlation coefficient —$|r|$ values.

[2] For CSM variables, mean, Q_{80}, and Q_{90} denote the mean, average value of the top 80% and top 90% pixels within each plot, respectively; for texture variables, COR, MEAN, and ENT are grey level co-occurrence matrix-based correlation, mean, and entropy textures, respectively.

Texture performance—The texture is produced from a local neighborhood of pixels in the spectral orthoimages, and is related to the spatial distribution of vegetation, shadow, and soil pixels [6]. Textural information can enhance the detection of spatial information independently of tone, thereby facilitating the identification of canopy structures, such as plant density and leaf area index [44], [45]. This has the potential to increase the detection of AGB [46]. While previous article on image textures has largely focused on forest biomass estimation using satellite images, the properties of textures make them highly appropriate for agricultural applications. The UAV-derived images provide remarkable information on the number and distribution of dark (vegetation and shadow pixels) and bright areas (soil pixels) with high spatial resolutions [47], and the high spatial resolution enables finer structural details can be detected [48]. Hence, the UAV-based textures with centimeter-level spatial resolution have the potential to accurately estimate crop biomass [10], [15].

It remains uncertain which textures and their combinations offer the greatest potential, due to the complexity and variability of textures across objects of interest, physiographic conditions, and the choice of window size [46]. The geometric characteristics of the remote sensing images taken from UAV cameras have geometric distortions, such as scale variation and displacement of terrain features [49], so the image overlap and spatial resolution affect the quality of orthoimages and thereby the texture features. The size of the moving window and the spatial resolution of UAV images are two factors that might affect the GLCM calculation. As the textures performed well in this article, spatial resolution might be the primary factor [15]. We suggest that texture shows higher resilience to variations in image quantity and spatial scales present in the UAV flight height compared to the CSM. As a result, the texture was found to provide more accurate AGB estimates at flight heights ranging from 4–8 cm in this article, compared to CSM. The relationships between texture variables and AGB across spatial scales also proved textures were lower sensitive to UAV flight height than CSM (Table IX).

Spectral performance—Spectral indices are built based on the understanding of complicated radiation and vegetation interactions. Leaf reflectance is relatively low in the visible ranges (400–700 nm) owing to the strong absorption by the photosynthetic pigments particularly the chlorophylls, whereas high reflectance exists in the NIR ranges because of internal leaf scattering and no absorption [50], [51]. The reflection of radiation from the surfaces of leaves does not provide any information about the interior of the leaves but may vary based on the species of vegetation and growing conditions [52]. The properties of leaves play a significant role in shaping important ecological processes related to the exchange of energy and matter, such as evapotranspiration, respiration, and photosynthesis activities [53], [54]. In addition to leaf properties, spectral indices are also impacted by canopy features, as the structure of the canopy affects the amount of incoming radiation through multiple scattering, absorption, and escape [55]. In comparison to textures and CSM, spectral indices possess a more comprehensive representation of vegetation properties at both the leaf and canopy levels, leading to more stable and accurate estimates of AGB, which can be also demonstrated in Table IX.

B. Design of Optimal UAV Observation Schemes

This article demonstrated that texture + spectral outperformed CSM + spectral, which could be explained by the better performance of textures than CSM in AGB estimation. However, this article only considered the effects of flight height on CSM generation, while other approaches could be alternatives to improve the performance of the CSM dataset, such as the lower flight height to obtain detailed information, increasing image overlaps [56], optimizing SfM algorithms [57], and conducting multidirection flight to mitigate the effects of shading problems [36]. Nevertheless, it should be highlighted that the textures exhibited a more robust performance than CSM in AGB estimation, which is preferred in practical applications. We inferred that the better performance of textures could be due to their ability to provide more features and details of objects than CSM. Generally, CSM is highly correlated with values and spatial variations of canopy height [9], so the CSM indicators contain rather monotonous crop information. However, textures have more indicators to characterize object features. For example, the entropy texture depicts the diversity of pixels within each plot and is very sensitive to clumpiness [58]; the mean and correlation textures are good at classification, and dissimilarly texture serves well for edge detection [59], [60].

Several studies have successfully applied optical-based structure information on crop parameter estimation, concluding that CSM/texture information boosted the estimation accuracy [4], consistent with this article. This is because spectral indices and textures or CSM information respond differently to the vegetation canopy structure characteristics, so their complementary information can improve AGB estimation [15]. For instance, Maimaitijiang et al. [9] used a Mapir Survey2 camera to generate CSMs for estimating soybean yield; it showed that canopy texture contributed to more accurate yield estimation. Yue et al. [15] used an RGB camera with a ground spatial resolution of

1 cm to generate various scale canopy textures via spatial resampling. Their results demonstrated that textures were insensitive to ground spatial resolution, and the integration of canopy texture and spectral information boosted estimation accuracy. The studies of Han et al. [2] and Bending et al. [16] demonstrated that integrating CSM into spectral data could also improve biomass estimation. Due to our primary focus on the effects of UAV flight height on AGB estimation and the observed decreased performance of the CSM derived from higher flight missions, we did not examine the impact of combining UAV spectral, texture, and CSM variables at different scales on AGB estimation.

Our results showed that the integration of multiscale data improved the performance of the spectral, texture, and their integrated dataset in AGB estimation, and the texture + spectral exhibited the best performance. UAV flight missions at multiple heights can provide more features of objects because the spatial pattern is scale-dependent, and the dominant factors might not keep consistent at distinct scales [61]. Although high spatial resolution can provide intricate details of objects, it also tends to include more environmental noise originating from factors, such as soil, weeds, and shadows. These additional elements have the potential to impact the spatial patterns and spectral characteristics of canopies as observed through UAV-based imaging. The elimination of these noises through the combination of data from different flight heights is likely the primary reason behind the improved performance of the texture and spectral indices. Pixels at coarse spatial resolutions might contain shadow and other elements, thus decreasing the reflectivity of shadow [36]. On the other side, observations at multiple flight heights are indirect multiangular measurements, which offer an approach to characterizing the anisotropy of reflectance [5]. Under such a context, the performance of the texture dataset could be improved via the integration of multiscale images. However, for CSM, errors from too coarse spatial resolutions and limited images could not be compensated by the data integration superiority.

As for practical conditions, overall, texture + spectral indices with moderate ground resolution (4–6 cm) are recommended for biomass estimation at the grain filling stage of wheat. However, another light optical sensor—the commercial RGB camera is often used in practice. It should be noted that RGB cameras have an extra-high spatial resolution, but they lack the RE and NIR bands which are vital spectral information for crop monitoring. In such a context, it is of great significance to explore how to compensate for this disadvantage of RGB cameras. Based on the results of this article, an alternative might be the multiscale textures, which exhibited satisfying AGB estimation accuracy. On the other hand, the multiscale data can lead to an augmented workload for image acquisition, especially for regions with a large area. While it should be noted that the multiscale data are not generally required under field conditions. Considering the current state and technologies of UAV remote sensing systems, multiscale textures might be more suited for monitoring vegetation on a smaller area or for crops with higher economic value.

In addition, both the data source and modeling algorithms determined a reliable estimation; the data source was explained by 69% of the observed variance for estimated variables and the model type only 28% [62]. Although the variables utilized in

machine and deep learning may differ, both rely on the same original data source, but albeit with distinct approaches to analysis and modeling. The inputs of RF and SVR are the average values of all pixels within a selected region of each plot, which may lead to distorting the properties of pure pixels whereas receiving the mixed signal of canopies, shadows, soil background, and other components on the land surface [56]. Furthermore, the machine-learning inputs should be initially filtered manually [10]. Consequently, model robustness and generalization might be reduced. In DCNN, the role of convolution and pooling layers is to find patterns in the input source, and the dense layers classify these features into appropriate categories [63]. No precalculation of features is needed for DCNN models since the convolutional layers of networks can automatically conduct the feature extraction operation, and optimal features are obtained in model training to alleviate biases in specific feature selection [64]. In addition, the raw images used in DCNN convey more information on crop growth status within pure pixels [7], [22]. Therefore, the DCNN model outperforms RF and SVR at high spatial scales, and DCNN was more sensitive to image spatial resolutions than RF and SVR. Nevertheless, it is challenging to give a general conclusion about which algorithm outperforms others, because complex factors should be considered together in practical applications, such as computing costs and model complexity.

C. Summary of Limitations

There were some limitations in the flight height and field scale due to technical limits or legislative restrictions. In particular, the restricted airspace range limited this article to four flight heights. Future articles should aim to explore the findings of this article at broader spatial scales by conducting investigations at higher UAV flight heights. We selected small-scale farmland to conduct the UAV experiment; this choice allowed us to have accurate and detailed field data (e.g., irrigation and fertilizer treatments) to represent the reality, which led to different crop biomass. However, the destructive harvest was relatively small because of the limited size of plots (0.5 m of a row). Thus, there are some uncertainties concerning the ground measurement of AGB. To facilitate sustainable agriculture and promote commercial uses of optimal UAV monitoring, research on practical large-scale farmland is needed to optimize flight height and monitoring ranges. In contrast, working with small-scale farmland can help alleviate uncertainties resulting from varying external environmental conditions, such as variations in sunlight angles and wind speeds, typically encountered during multiple UAV flight missions. This is because the flight missions can be completed within a relatively brief time frame. However, for larger farmland areas, an alternative solution to this challenge could be the implementation of simultaneous multi-UAV flight missions.

Additionally, it is worth noting that the UAV monitoring in this article was specifically conducted during the grain filling stage of wheat, a period when the crop height remains relatively constant while the AGB continues to increase. Consequently, UAV variables that primarily capture crop height-related features, such as the CSM used in this article, may exhibit reduced

sensitivity to AGB and consequently demonstrate relatively poorer performance. It has been indicated in previous articles that the applicability of UAV-based indicators varies depending on the stage of crop development [10]. To further validate our findings, it is recommended to encompass UAV monitoring throughout different phenological stages of the crop, allowing for a comprehensive assessment of our findings.

VI. Conclusion

This article assessed the impact of changes in flight height and integration of multiscale sensing information on estimating wheat AGB. According to our findings, the following conditions hold:

1) The effects of UAV flight height on AGB estimation performance were different across UAV datasets; the sensitivity of dataset performance to UAV flight height was CSM > textures > spectral indices, as the RMSE values of spectral, texture, CSM, texture + spectral, and CSM + spectral dataset-based estimation using datasets at 120 m decreased by around 25%, 41%, 48%, 24%, and 48% of those using datasets at 30 m, respectively.
2) DCNN performed better than two machine-learning approaches (RF and SVR) in AGB estimation, particularly at the high spatial resolution of images. At the same time, the DCNN was more sensitive to UAV flight height; from 30 to 120 m, the RMSE values increased by around 32%, 31%, and 47% for RF, SVR, and DCNN models, respectively.
3) Integration of multiscale UAV data improved the AGB estimation accuracy of the spectral, texture, and spectral + texture datasets while decreasing the performance of CSM and CSM + spectral datasets.
4) Two UAV dataset strategies are recommended for wheat AGB estimation at the grain filling stages in practical applications, i.e., UAV texture + spectral derived from images with moderate spatial resolutions (4–6 cm) and the integrated multiscale textures. This straightforward optical-based UAV agromonitoring scheme can help farmers and farm managers reduce agronomic monitoring costs and optimize practical management.

Acknowledgment

References

[1] L. A. Suarez, A. Robson, J. McPhee, J. O'Halloran, and C. van Sprang, "Accuracy of carrot yield forecasting using proximal hyperspectral and satellite multispectral data," *Precis. Agriculture*, vol. 21, no. 6, pp. 1304–1326, Dec. 2020, doi: 10.1007/s11119-020-09722-6.

[2] L. Han et al., "Modeling maize above-ground biomass based on machine learning approaches using UAV remote-sensing data," *Plant Methods*, vol. 15, no. 1, Feb. 2019, Art. no. 10, doi: 10.1186/s13007-019-0394-z.

[3] Y. Fu et al., "Improved estimation of winter wheat aboveground biomass using multiscale textures extracted from UAV-based digital images and hyperspectral feature analysis," *Remote Sens.*, vol. 13, no. 4, Jan. 2021, Art. no. 4, doi: 10.3390/rs13040581.

[4] Y. Liu, S. Liu, J. Li, X. Guo, S. Wang, and J. Lu, "Estimating biomass of winter oilseed rape using vegetation indices and texture metrics derived from UAV multispectral images," *Comput. Electron. Agriculture*, vol. 166, Nov. 2019, Art. no. 105026, doi: 10.1016/j.compag.2019.105026.

[5] H. Chen, W. Huang, W. Li, Z. Niu, L. Zhang, and S. Xing, "Estimation of LAI in winter wheat from multi-angular hyperspectral VNIR data: Effects of view angles and plant architecture," *Remote Sens.*, vol. 10, no. 10, Oct. 2018, Art. no. 1630, doi: 10.3390/rs10101630.

[6] R. Colombo, D. Bellingeri, D. Fasolini, and C. M. Marino, "Retrieval of leaf area index in different vegetation types using high resolution satellite data," *Remote Sens. Environ.*, vol. 86, no. 1, pp. 120–131, 2003, doi: 10.1016/S0034-4257(03)00094-4.

[7] Q. Yang, L. Shi, J. Han, Y. Zha, and P. Zhu, "Deep convolutional neural networks for rice grain yield estimation at the ripening stage using UAV-based remotely sensed images," *Field Crops Res.*, vol. 235, pp. 142–153, Apr. 2019, doi: 10.1016/j.fcr.2019.02.022.

[8] J. Yue, G. Yang, Q. Tian, H. Feng, K. Xu, and C. Zhou, "Estimation of winter wheat above-ground biomass using unmanned aerial vehicle-based snapshot hyperspectral sensor and crop height improved models," *Remote Sens.*, vol. 9, no. 7, Jul. 2017, Art. no. 708, doi: 10.3390/rs9070708.

[9] M. Maimaitijiang, V. Sagan, P. Sidike, S. Hartling, F. Esposito, and F. B. Fritschi, "Soybean yield prediction from UAV using multimodal data fusion and deep learning," *Remote Sens. Environ.*, vol. 237, Feb. 2020, Art. no. 111599, doi: 10.1016/j.rse.2019.111599.

[10] W. Zhu et al., "UAV-based indicators of crop growth are robust for distinct water and nutrient management but vary between crop development phases," *Field Crops Res.*, vol. 284, Aug. 2022, Art. no. 108582, doi: 10.1016/j.fcr.2022.108582.

[11] C. T. de Almeida et al., "Combining LiDAR and hyperspectral data for aboveground biomass modeling in the Brazilian Amazon using different regression algorithms," *Remote Sens. Environ.*, vol. 232, Oct. 2019, Art. no. 111323, doi: 10.1016/j.rse.2019.111323.

[12] X. Li, Y. Sun, and Q. Zhang, "Extraction of sea ice cover by Sentinel-1 SAR based on support vector machine with unsupervised generation of training data," *IEEE Trans. Geosci. Remote Sens.*, vol. 59, no. 4, pp. 3040–3053, Apr. 2021, doi: 10.1109/TGRS.2020.3007789.

[13] S. W. Myint, P. Gober, A. Brazel, S. Grossman-Clarke, and Q. Weng, "Per-pixel vs. object-based classification of urban land cover extraction using high spatial resolution imagery," *Remote Sens. Environ.*, vol. 115, no. 5, pp. 1145–1161, May 2011, doi: 10.1016/j.rse.2010.12.017.

[14] H. Zheng et al., "Improved estimation of rice aboveground biomass combining textural and spectral analysis of UAV imagery," *Precis. Agriculture*, vol. 20, no. 3, pp. 611–629, Jun. 2019, doi: 10.1007/s11119-018-9600-7.

[15] J. Yue, G. Yang, Q. Tian, H. Feng, K. Xu, and C. Zhou, "Estimate of winter-wheat above-ground biomass based on UAV ultrahigh-ground-resolution image textures and vegetation indices," *ISPRS J. Photogramm.*, vol. 150, pp. 226–244, Apr. 2019, doi: 10.1016/j.isprsjprs.2019.02.022.

[16] J. Bendig et al., "Combining UAV-based plant height from crop surface models, visible, and near infrared vegetation indices for biomass monitoring in barley," *Int. J. Appl. Earth Observ.*, vol. 39, pp. 79–87, Jul. 2015, doi: 10.1016/j.jag.2015.02.012.

[17] J. P. Dandois, M. Olano, and E. C. Ellis, "Optimal altitude, overlap, and weather conditions for computer vision UAV estimates of forest structure," *Remote Sens.*, vol. 7, no. 10, Oct. 2015, Art. no. 10, doi: 10.3390/rs71013895.

[18] D. Yu et al., "Improvement of sugarcane yield estimation by assimilating UAV-derived plant height observations," *Eur. J. Agronomy*, vol. 121, Nov. 2020, Art. no. 126159, doi: 10.1016/j.eja.2020.126159.

[19] G. Modica, G. Messina, and G. De Luca, "Monitoring the vegetation vigor in heterogeneous citrus and olive orchards. A multiscale object-based approach to extract trees' crowns from UAV multispectral imagery," *Comput. Electron. Agriculture*, vol. 175, Aug. 2020, Art. no. 105500, doi: 10.1016/j.compag.2020.105500.

[20] R. Pu, "Assessing scaling effect in downscaling land surface temperature in a heterogenous urban environment," *Int. J. Appl. Earth Observ.*, vol. 96, Apr. 2021, Art. no. 102256, doi: 10.1016/j.jag.2020.102256.

[21] Q. Yuan et al., "Deep learning in environmental remote sensing: Achievements and challenges," *Remote Sens. Environ.*, vol. 241, May 2020, Art. no. 111716, doi: 10.1016/j.rse.2020.111716.

[22] D. Yu et al., "Deep convolutional neural networks for estimating maize above-ground biomass using multi-source UAV images: A comparison with traditional machine learning algorithms," *Precis. Agriculture*, vol. 24, pp. 92–113, Jul. 2022, doi: 10.1007/s11119-022-09932-0.

[23] Y. Liu, H. Feng, Q. Sun, F. Yang, and G. Yang, "Estimation study of above ground biomass in potato based on UAV digital images with different resolutions," *Spectrosc. Spectral Anal.*, vol. 41, no. 5, pp. 1470–1476, May 2021, doi: 10.3964/j.issn.1000-0593(2021)05-1470-07.

[24] W. Zhu et al., "Estimating maize above-ground biomass using 3D point clouds of multi-source unmanned aerial vehicle data at multi-spatial scales," *Remote Sens.*, vol. 11, no. 22, Jan. 2019, Art. no. 2678, doi: 10.3390/rs11222678.

[25] D. Domingo, H. O. Ørka, E. Næsset, D. Kachamba, and T. Gobakken, "Effects of UAV image resolution, camera type, and image overlap on accuracy of biomass predictions in a tropical woodland," *Remote Sens.*, vol. 11, no. 8, Jan. 2019, Art. no. 8, doi: 10.3390/rs11080948.

[26] J. ten Harkel, H. Bartholomeus, and L. Kooistra, "Biomass and crop height estimation of different crops using UAV-based lidar," *Remote Sens.*, vol. 12, no. 1, Jan. 2020, Art. no. 1, doi: 10.3390/rs12010017.

[27] E. F. Berra, R. Gaulton, and S. Barr, "Assessing spring phenology of a temperate woodland: A multiscale comparison of ground, unmanned aerial vehicle and Landsat satellite observations," *Remote Sens. Environ.*, vol. 223, pp. 229–242, 2019, doi: 10.1016/j.rse.2019.01.010.

[28] G. B. M. Heuvelink, "Interpolation of spatial data: Some theory for kriging," *Geoderma*, vol. 96, no. 1–2, pp. 153–154, May 2000, doi: 10.1016/S0016-7061(00)00010-0.

[29] R. M. Haralick, K. Shanmugam, and I. Dinstein, "Textural features for image classification," *IEEE Trans. Syst., Man, Cybern.*, vol. SMC-3, no. 6, pp. 610–621, Nov. 1973, doi: 10.1109/TSMC.1973.4309314.

[30] C. Daughtry, C. Walthall, M. Kim, E. Brown de Colstoun, and J. E. Mc-Murtrey III, "Estimating corn leaf chlorophyll concentration from leaf and canopy reflectance," *Remote Sens. Environ.*, vol. 74, no. 2, pp. 229–239, Nov. 2000, doi: 10.1016/S0034-4257(00)00113-9.

[31] K. Yu, V. Lenz-Wiedemann, X. Chen, and G. Bareth, "Estimating leaf chlorophyll of barley at different growth stages using spectral indices to reduce soil background and canopy structure effects," *ISPRS-J. Photogramm. Remote Sens.*, vol. 97, pp. 58–77, Nov. 2014, doi: 10.1016/j.isprsjprs.2014.08.005.

[32] A. Krizhevsky, I. Sutskever, and G. E. Hinton, "ImageNet classification with deep convolutional neural networks," *Commun. ACM*, vol. 60, no. 6, pp. 84–90, May 2017, doi: 10.1145/3065386.

[33] L. Breiman, "Random forests," *Mach. Learn.*, vol. 45, no. 1, pp. 5–32, 2001, doi: 10.1023/A:1010933404324.

[34] M. Belgiu and L. Drăguţ, "Random forest in remote sensing: A review of applications and future directions," *ISPRS J. Photogramm.*, vol. 114, pp. 24–31, Apr. 2016, doi: 10.1016/j.isprsjprs.2016.01.011.

[35] M. Awad and R. Khanna, "Support vector regression," 2015. Accessed: Jan. 18, 2022. [Online]. Available: https://link.springer.com/chapter/10.1007/978-1-4302-5990-9_4

[36] C. H. W. De Souza, R. A. C. Lamparelli, J. V. Rocha, and P. S. G. Magalhães, "Height estimation of sugarcane using an unmanned aerial system (UAS) based on structure from motion (SfM) point clouds," *Int. J. Appl. Earth Observ.*, vol. 38, no. 8–10, pp. 2218–2230, May 2017, doi: 10.1080/01431161.2017.1285082.

[37] E. Sanz-Ablanedo, J. H. Chandler, J. R. Rodríguez-Pérez, and C. Ordóñez, "Accuracy of unmanned aerial vehicle (UAV) and SfM photogrammetry survey as a function of the number and location of ground control points used," *Remote Sens.*, vol. 10, no. 10, Oct. 2018, Art. no. 10, doi: 10.3390/rs10101606.

[38] M. Hirschmugl, M. Ofner, J. Raggam, and M. Schardt, "Single tree detection in very high resolution remote sensing data," *Remote Sens. Environ.*, vol. 110, no. 4, pp. 533–544, 2007, doi: 10.1016/j.rse.2007.02.029.

[39] J. Geipel, J. Link, and W. Claupein, "Combined spectral and spatial modeling of corn yield based on aerial images and crop surface models acquired with an unmanned aircraft system," *Remote Sens.*, vol. 6, no. 11, pp. 10335–10355, Oct. 2014, doi: 10.3390/rs61110335.

[40] S. Harwin and A. Lucieer, "Assessing the accuracy of georeferenced point clouds produced via multi-view stereopsis from unmanned aerial vehicle (UAV) imagery," *Remote Sens.*, vol. 4, no. 6, Jun. 2012, Art. no. 6, doi: 10.3390/rs4061573.

[41] J. R. Kiniry, C. A. Jones, J. C. O'toole, R. Blanchet, M. Cabelguenne, and D. A. Spanel, "Radiation-use efficiency in biomass accumulation prior to grain-filling for five grain-crop species," *Field Crops Res.*, vol. 20, no. 1, pp. 51–64, Feb. 1989, doi: 10.1016/0378-4290(89)90023-3.

[42] D. W. Stewart, C. Costa, L. M. Dwyer, D. L. Smith, R. I. Hamilton, and B. L. Ma, "Canopy structure, light interception, and photosynthesis in Maize," *Agronomy J.*, vol. 95, no. 6, pp. 1465–1474, 2003, doi: 10.2134/agronj2003.1465.

[43] A. Viña and A. A. Gitelson, "New developments in the remote estimation of the fraction of absorbed photosynthetically active radiation in crops," *Geophys. Res. Lett.*, vol. 32, 2005, Art. no. 17, doi: 10.1029/2005GL023647.

[44] R. Pu and J. Cheng, "Mapping forest leaf area index using reflectance and textural information derived from WorldView-2 imagery in a mixed natural forest area in Florida, US," *Int. J. Appl. Earth Observ.*, vol. 42, pp. 11–23, Oct. 2015, doi: 10.1016/j.jag.2015.05.004.

[45] M. A. Wulder, E. F. LeDrew, S. E. Franklin, and M. B. Lavigne, "Aerial image texture information in the estimation of Northern deciduous and mixed wood forest leaf area index (LAI)," *Remote Sens. Environ.*, vol. 64, no. 1, pp. 64–76, Apr. 1998, doi: 10.1016/S0034-4257(97)00169-7.

[46] L. R. Sarker and J. E. Nichol, "Improved forest biomass estimates using ALOS AVNIR-2 texture indices," *Remote Sens. Environ.*, vol. 115, no. 4, pp. 968–977, Apr. 2011, doi: 10.1016/j.rse.2010.11.010.

[47] Y. Zhou et al., "Diagnosis of winter-wheat water stress based on UAV-borne multispectral image texture and vegetation indices," *Agricultural Water Manage.*, vol. 256, 2021, Art. no. 107076, doi: 10.1016/j.agwat.2021.107076.

[48] G. J. Hay, K. O. Niemann, and G. F. McLean, "An object-specific image-texture analysis of H-resolution forest imagery," *Remote Sens. Environ.*, vol. 55, no. 2, pp. 108–122, Feb. 1996, doi: 10.1016/0034-4257(95)00189-1.

[49] E. J. Yoo and D. C. Lee, "True orthoimage generation by mutual recovery of occlusion areas," *GISci. Remote Sens.*, vol. 53, no. 2, pp. 227–246, 2016, doi: 10.1080/15481603.2015.1128629.

[50] E. B. Knipling, "Physical and physiological basis for the reflectance of visible and near-infrared radiation from vegetation," *Remote Sens. Environ.*, vol. 1, no. 3, pp. 155–159, Jun. 1970, doi: 10.1016/S0034-4257(70)80021-9.

[51] S. V. Ollinger, "Sources of variability in canopy reflectance and the convergent properties of plants," *New Phytol.*, vol. 189, no. 2, pp. 375–394, 2011, doi: 10.1111/j.1469-8137.2010.03536.x.

[52] Y. Knyazikhin et al., "Hyperspectral remote sensing of foliar nitrogen content," *PNAS*, vol. 110, no. 3, pp. E185–E192, Jan. 2013, doi: 10.1073/pnas.1210196109.

[53] I. Pôças, A. Calera, I. Campos, and M. Cunha, "Remote sensing for estimating and mapping single and basal crop coefficients: A review on spectral vegetation indices approaches," *Agricultural Water Manage.*, vol. 233, Apr. 2020, Art. no. 106081, doi: 10.1016/j.agwat.2020.106081.

[54] Q. Wang and P. Li, "Hyperspectral indices for estimating leaf biochemical properties in temperate deciduous forests: Comparison of simulated and measured reflectance data sets," *Ecol. Indicators*, vol. 14, no. 1, pp. 56–65, Mar. 2012, doi: 10.1016/j.ecolind.2011.08.021.

[55] Y. Zeng et al., "Optical vegetation indices for monitoring terrestrial ecosystems globally," *Nature Rev. Earth Environ.*, vol. 3, no. 7, Jul. 2022, Art. no. 7, doi: 10.1038/s43017-022-00298-5.

[56] J. Frey, K. Kovach, S. Stemmler, and B. Koch, "UAV photogrammetry of forests as a vulnerable process: A sensitivity analysis for a structure from motion RGB-image pipeline," *Remote Sens.*, vol. 10, no. 6, Jun. 2018, Art. no. 6, doi: 10.3390/rs10060912.

[57] S. Jiang, C. Jiang, and W. Jiang, "Efficient structure from motion for large-scale UAV images: A review and a comparison of SfM tools," *ISPRS-J. Photogramm. Remote Sens.*, vol. 167, pp. 230–251, 2020, doi: 10.1016/j.isprsjprs.2020.04.016.

[58] T. M. Kuplich, P. J. Curran, and P. M. Atkinson, "Relating SAR image texture to the biomass of regenerating tropical forests," *Int. J. Appl. Earth Observ.*, vol. 26, no. 21, pp. 4829–4854, 2005, doi: 10.1080/01431160500239107.

[59] P. M. Treitz, P. J. Howarth, O. R. Filho, and E. D. Soulis, "Agricultural crop classification using SAR tone and texture statistics," *Can. J. Remote Sens.*, vol. 26, no. 1, pp. 18–29, 2000, doi: 10.1080/07038992.2000.10874751.

[60] S. Wan and S. Chang, "Crop classification with WorldView-2 imagery using support vector machine comparing texture analysis approaches and grey relational analysis in Jianan Plain, Taiwan," *Int. J. Appl. Earth Observ.*, vol. 40, no. 21, pp. 8076–8092, 2019, doi: 10.1080/01431161.2018.1539275.

[61] H. Wu and Z. Li, "Scale issues in remote sensing: A review on analysis, processing and modeling," *Sensors*, vol. 9, no. 3, Mar. 2009, Art. no. 3, doi: 10.3390/s90301768.

[62] A. Masjedi, M. M. Crawford, N. R. Carpenter, and M. R. Tuinstra, "Multi-temporal predictive modelling of Sorghum biomass using UAV-based hyperspectral and LiDAR data," *Remote Sens.*, vol. 12, no. 21, Nov. 2020, Art. no. 3587, doi: 10.3390/rs12213587.

[63] A. Bouguettaya, H. Zarzour, A. Kechida, and A. M. Taberkit, "Deep learning techniques to classify agricultural crops through UAV imagery: A review," *Neural Comput. Appl.*, vol. 34, no. 12, pp. 9511–9536, Jun. 2022, doi: 10.1007/s00521-022-07104-9.

[64] P. Nevavuori, N. Narra, and T. Lipping, "Crop yield prediction with deep convolutional neural networks," *Comput. Electron. Agriculture*, vol. 163, Aug. 2019, Art. no. 104859, doi: 10.1016/j.compag.2019.104859.

Wanxue Zhu received the Ph.D. degree in ecology from the University of Chinese Academy of Sciences, Beijing, China, in 2022.

She is currently a Scientific Researcher with the Department of Crop Sciences, University of Göttingen, Göttingen, Germany. She was a Visiting Scholar with the University of Göttingen and Leibniz Centre for Agricultural Landscape Research. Her research interests include the application of remote sensing in agriculture, such as crop phenotyping via multisource unmanned aerial vehicle remote sensing observation, optimization of UAV monitoring schemes for crop growth, and diagnosis of environmental stresses of crop growth via the integration of UAV and satellite remote sensing. Her research interests also include developing dynamic irrigation extent of Europe using process-based model simulation and remote sensing approach, for better quantifying differences in water use between dry and wet years.

Ehsan Eyshi Rezaei received the Ph.D. degree in agricultural sciences from the University of Bonn, Bonn, Germany, in 2016.

He is currently a Tenure Track Scientist with the Leibniz Centre for Agricultural Landscape Research. He has previously worked as a Postdoc Research Scientist with both the University of Bonn and the University of Göttingen, Göttingen, Germany. His research interests include interactions among environment × genotype × management on crop growth and development. He employs state-of-the-art process-based crop models and sensing technologies to gain a comprehensive understanding of these interactions. He is dedicated to developing innovative modeling routines to disentangle the effects of multiple stresses (primarily heat and drought) in the context of climate change and variability on cropping systems. Through these efforts, he aims to contribute to designing effective climate change adaptation strategies for the agricultural sector.

Hamideh Nouri received Ph.D. degree in civil engineering from the University of South Australia, Adelaide, Australia, in 2014.

He is currently a Senior Project Manager with the Institute Partner, Department for Environment and Water. She has strong collaborations with several universities worldwide, has supervised tens of Ph.D. & M.Sc. students, mentored young professionals, and authored/coauthored more than 100 articles and reports. She has worked with the United Nations, European Union, and U.S. Geological Survey for several years and the public and private sectors in different countries, led many high-performing teams and managed hundreds of national and international water-related projects. She has a background in water engineering and management and hands-on experience in integrated water resources management, water-food security nexus, water policy & governance, urban water, and climate change adaptation & mitigation.

Zhigang Sun received the Ph.D. degree in environmental modeling and remote sensing from the University of Tsukuba, Tsukuba, Japan, in 2008.

He is currently a Professor with the Institute of Geographic Sciences and Natural Resources Research, Chinese Academy of Sciences, Beijing, China. He has previously worked as a Postdoc Research Scientist with the University of Connecticut, Storrs, CT, USA, and as an Associate Researcher with the Center for Regional Environmental Research of Japan. His research interests include multiscale monitoring, simulation, and assessment of agroecosystems; regional diagnosis and spatiotemporal optimization of agroecosystems; agroecosystem responses and adaptations to climate change; micro-UAVs and their applications in agriculture; remote sensing, Big Data, and their applications in agriculture; and agricultural system optimization and regional sustainable development.

Jing Li received the Ph.D. degree from the Ecological and Environmental Research Center, Chinese Academy of Sciences, Beijing, China, in 2010.

She is currently an Associate Professor with the Institute of Geographic Sciences and Natural Resources Research, Chinese Academy of Sciences. She was previously a Visiting Scholar with the Lancaster Environment Centre, Lancaster University, Lancaster, U.K. Her research interests include soil health and agricultural ecosystem management, including key ecological processes and regional risks related to soil nitrogen and heavy metals. Her work also involves regulating nutrient balance in farmlands and constructing ecological agricultural models.

Danyang Yu received the Ph.D. degree in agro-hydrological science from the University of Wuhan, Wuhan, China, in 2022.

He is currently a Postdoctor Researcher with the Faculty Geo-Information Science and Earth Observation, University of Twente, Enschede, The Netherlands. His research interests include interactions among radiation transfer, soil water/heat movement, and plant growth in Soil–Plant–Atmosphere Continuum system. He employs state-of-the-art process-based terrestrial ecosystem models and remote sensing technologies to gain a comprehensive understanding of these interactions. He is dedicated to fusing multiple-source information from remote sensing data into the modeling process to reduce the uncertainties of model predictions on cropping or ecosystem systems. Through these efforts, he aims to contribute to understanding the relationships between plant physiology and spectrum response.

Stefan Siebert received the Ph.D. degree in agricultural sciences from the University of Kassel, Kassel, Germany, in 2005.

He is currently a Professor of Agronomy with the Department of Crop Sciences, University of Göttingen, Göttingen, Germany, and the Head of the Division Agronomy. He has previously worked as a Postdoc Research Scientist with the University of Frankfurt (Main), Frankfurt, Germany and University of Bonn, Bonn, Germany. His research interests include analysis of interactions between crop production systems and their environment by data analysis, modeling, sensing, and field experimentation. Large-scale datasets and model components are developed to assess the interaction between resource use, crop management, and crop productivity. His research interests also include crop modeling in general (phenology, drought and heat stress, and crop yields), modeling of virtual water flows, climate impact, climate adaptation, and the alteration of ecosystems by anthropogenic impacts.